

# On-Board Single-Phase Integrated Electric Vehicle Charger With V2G Functionality

Sepehr Semsar , *Student Member, IEEE*, Theodore Soong, *Member, IEEE*, and Peter W. Lehn, *Senior Member, IEEE*

**Abstract**—Mass adoption of electric vehicles (EVs) is contingent on the availability of charging infrastructure. One solution to this issue is the introduction of on-board fast chargers, but such solutions typically require the installation of additional magnetic components that increase EV mass. An alternative approach is the dynamic redeployment of drivetrain components for charging when the vehicle is stationary. This article proposes an on-board single-phase charger that reuses the traction inverter and motor. The system consists of a dual-inverter drivetrain, which affords higher voltage charging compared to conventional systems. In addition, the system is able to operate bidirectionally and operate at any power factor for grid support services with real and reactive power exchange without subjecting the motor to low frequency harmonic currents. Experimental tests demonstrated operation at 19.2 kW using a 110-kW EV motor and a full-scale, state-of-the-art, dual-inverter drive prototype. Measured peak efficiencies of over 97% demonstrate the viability of integrated charging in a real-world scenario.

**Index Terms**—Battery chargers, dual-inverter drive, electric vehicles, integrated on-board chargers, motor drives.

## I. INTRODUCTION

A MAJOR obstacle against the mass adoption of electric vehicles (EVs) is the availability and charging speed of EV charging infrastructure. EV manufacturers include on-board chargers (OBCs) as a convenient means for charging; however, these are typically discrete power electronic converters installed into the vehicle with a low power rating [2]. Higher power solutions are not feasible due to the added cost, size, and weight penalty. An alternative approach to installing separate OBCs is to redeploy existing drivetrain components to serve as a part of the charging system. This notion of integrated charging is something that has gained a lot of attention beginning in the early 1990s [3]–[5] since it effectively reduces the weight, volume, and cost while simultaneously increasing the charging power [2]–[13]. The traction inverter and motor would normally only be used as a drive when the vehicle is in motion, but they can also be redeployed to enable single-phase charging when stationary.

Manuscript received June 15, 2019; revised September 17, 2019 and January 23, 2020; accepted March 7, 2020. Date of publication March 19, 2020; date of current version July 20, 2020. This paper was presented in part at the 2018 International Power Electronics Conference, Niigata, Japan, May 2018 [1]. Recommended for publication by Associate Editor Mehdi Ferdowsi. (*Corresponding author: Sepehr Semsar.*)

The authors are with the Department of Electrical and Computer Engineering, University of Toronto, Toronto, ON M5S 3G4, Canada (e-mail: sep.semsar@mail.utoronto.ca; theodore.soong@mail.utoronto.ca; lehn@ecf.utoronto.ca). Color versions of one or more of the figures in this article are available online at <http://ieeexplore.ieee.org>.

Digital Object Identifier 10.1109/TPEL.2020.2982326

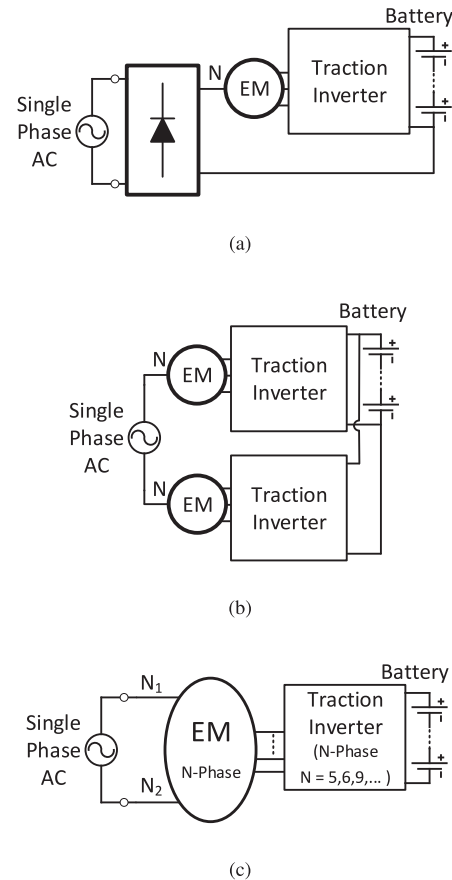


Fig. 1. Previously proposed integrated single-phase chargers. (a) PFC boost charger [9]. (b) Integrated charger using dual motor drive [10]. (c) Multiphase integrated charger [11].

Examples of some recently proposed integrated single-phase OBCs are shown in Fig. 1 where they utilize both the traction inverter and motor to achieve higher power charging. The simplest solution, proposed in [9] and shown in Fig. 1(a), uses a diode rectifier in tandem with the traction inverter to operate as a power factor correction (PFC) converter. While simple, this solution suffers from disadvantages typical of PFC-type converters, such as low frequency harmonic currents in magnetic elements and high switching frequency requirements. Particularly, the switching frequency requirements are problematic for large traction inverters. The approach suggested in [10] is a viable solution for drivetrains with dual motors, as shown in Fig. 1(b), where the single-phase ac grid is directly connected to the neutrals of two motors, while the system shares a single battery. This solution

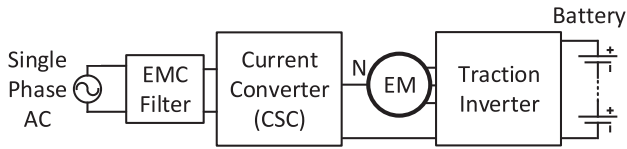


Fig. 2. Renault's integrated charger [14], [15].

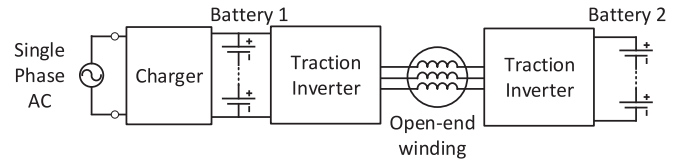
would be limited to higher end vehicles, potentially out of reach for many early EV adopters. An alternative solution employs a multiphase drive where the ac grid can be connected to the neutrals of the multiphase machine, as shown in Fig. 1(c) and suggested by [11]. This topology requires a specialized motor and inverter which are not commonly used for EVs, requiring custom machine design and power electronic modules. A state-of-the-art integrated charger in commercial production is the Renault Zoe's Chameleon charger, which is likely based on [14], [15]. As shown in Fig. 2, the charger requires an additional front-end current source converter as well as an electromagnetic compatibility filter, making it a somewhat complex and bulky system.

The aforementioned topologies consist of a single inverter per motor and a single battery, typically in the 300–450 V range. This has the disadvantage of reducing the grid voltage compatibility, as the battery voltage in its lowest state of charge (SoC) must exceed the peak of the ac grid voltage.

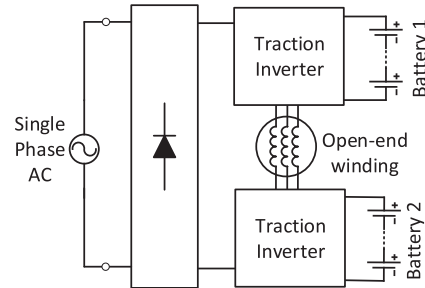
Dual-inverter drives are of interest due to their ability to drive a higher voltage motor using two conventional lower voltage traction inverters [16], [17], not only increasing efficiency but also improving grid voltage compatibility in integrated charging applications. Specifically, the dual-inverter drive functions as a single multilevel drive, resulting in lower harmonics and  $\frac{dv}{dt}$  stresses [16].

A complication of dual-inverter drive systems is the need to charge two separate batteries. To charge from an ac grid, solutions such as [12], shown in Fig. 3(a), use a separate OBC that charges the first battery while the dual inverters are used to charge the second battery. This implies that the high voltage advantage leveraged during motoring is not exploited when charging, whilst a slow and costly discrete OBC is still required. This can be remedied by connecting the charging terminals across the differential nodes of the dual-inverter drive as in [21], which utilizes the full voltage potential of the system both when motoring and charging. However, [21] only demonstrated viability in charging from dc sources since the dual-inverter drive is operated as a dc/dc converter. This idea was expanded in [22], where a diode rectifier was added to [21] and the dc/dc converter was operated as a PFC-type converter, as shown in Fig. 3(b). This PFC-type operation is similar to that in [9], as depicted in Fig. 1(a), but leverages the dual-inverter configuration to charge from higher voltage ac networks. However, high frequency switching requirements from the traction inverters and harmonic losses (due to conducting a rectified sinusoidal current) within the machine remain.

This article proposes a modification to the dual-inverter drive charger such that it eliminates the need for fast switching of the large traction inverters while conducting sinusoidal current within the machine. A comparison between the different



(a)



(b)

Fig. 3. Previously proposed dual-inverter drive integrated single-phase chargers. (a) A semi-integrated dual-inverter drive charging solution [12]. (b) Integrated PFC charger using dual-inverter drive [22].

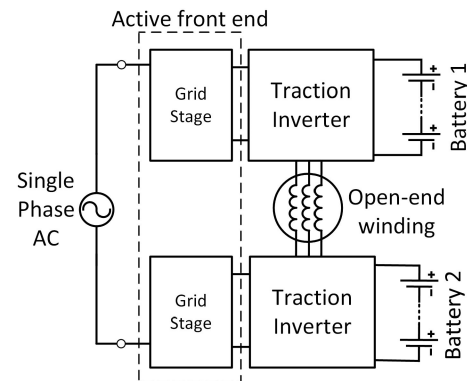


Fig. 4. Proposed integrated single-phase charger.

types of charging technologies is provided in Table I, which highlights some of the differences between integrated versus nonintegrated chargers as well as the advantages of the proposed charger. This article builds upon the previously published conference paper [1], with more details regarding the control scheme, improved modulation scheme for improved performance/efficiency, simulation results demonstrating charging from a 480 V grid, and experimental results demonstrating charging at 19.2 kW using a full-scale prototype utilizing a permanent magnet (PM) EV machine.

## II. PROPOSED TOPOLOGY

The proposed on-board single-phase charger is shown in Fig. 4. The charger is composed of four major parts: the motor, traction inverters, batteries, and the active front end (AFE). The AFE consists of two grid stages. During charging, the leakage inductance of the motor is used to avoid installation

TABLE I  
COMPARISON OF SINGLE PHASE ON-BOARD CHARGER (OBC) TECHNOLOGIES

Charger	Charging Power	Voltage Range	Size/Mass	Isolation	Bidirectional
Brusa OBC [18]	7.2kW	200-250 $V_{ac}$	Medium	Yes	No
Tesla OBC [19]	19.2kW	115-240 $V_{ac}$	High	Yes	No
Renault Integrated charger [20]	7.4kW	230 $V_{ac}$	Low-medium	No	Yes
Proposed Integrated charger	19.2kW	115-480 $V_{ac}$	Low	No	Yes

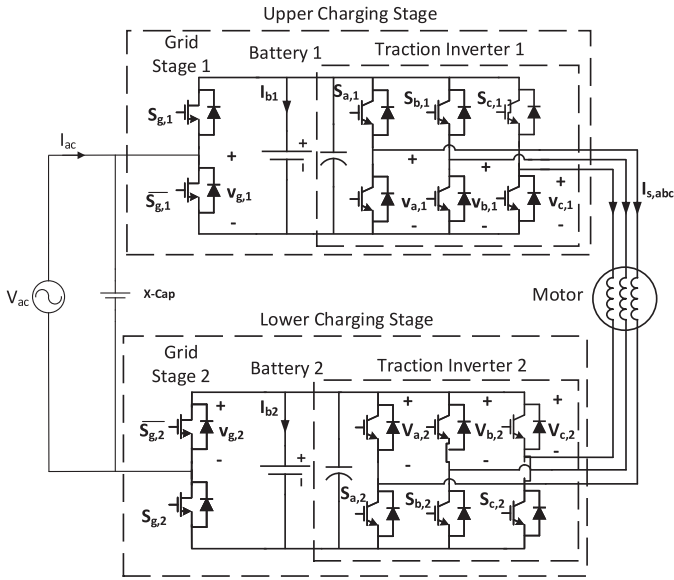


Fig. 5. Schematic of proposed integrated single-phase charger.

of additional magnetic components for charging. The only additional components are the grid stages, which would be used in conjunction with the traction inverters to charge the batteries from a single-phase ac grid. The grid stages allow the system to produce bipolar ac voltages at its input, up to a maximum voltage equal to the sum of the batteries 1 and 2 voltages. This is what enables increased grid voltage support. A detailed schematic of the proposed charger is shown in Fig. 5. It can be seen that the grid stages are implemented with a half-bridge, with the grid input being the switching nodes of the two half-bridges.

The charger is capable of bidirectional power flow at any power factor making it suitable for vehicle-to-grid (V2G) applications in addition to EV charging. The EV charger can therefore provide grid services like load leveling, peak shaving, frequency control, operate as a back-up power supply, etc. In addition, the system is capable of providing reactive power for grid voltage support. As an added benefit, the system is capable of fault blocking capabilities in case of fault events, allowing rapid electronic protection against faults within either the grid or motor. If only unity power factor charging operation were desired, each grid stage may be replaced with diodes without changes to the charger's principle of operation.

The ac power outlet is directly connected to the proposed on-board integrated charge and drive system. While this charger

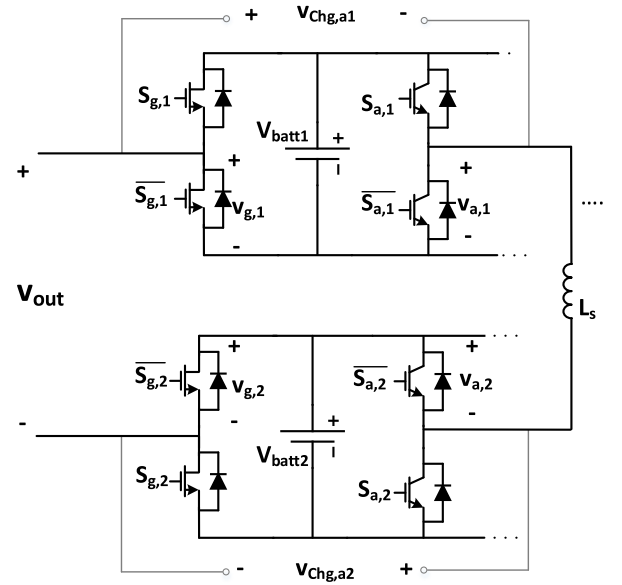


Fig. 6. Simplified system schematic.

is not galvanically isolated from the grid, it has been shown that the safety benefits offered by galvanic isolation can be replicated using various protective circuits such as the one shown in [23]. However, if absolutely required, an isolating transformer can be installed at the charging station. This implies that minimal charging infrastructure is needed for the charging station, limited to either a cable or cable with isolation transformer. This configuration also retains the dc fast charging capability proposed in [21] and is thus capable of either ac or dc charging.

#### A. Operating Principle

The integrated OBC can be divided symmetrically into upper and lower charging stages. Each charging stage consists of a traction inverter, battery, and grid stage, as labeled in Fig. 5. An open-winding motor is connected between the upper and lower charging stages, and its inductance is used as the filter for the charger. In this configuration, torque generation is prevented by running only zero sequence currents through the machine. This essentially means that the three phases of the traction inverter must operate identically. A simplified model of the system is shown in Fig. 6, considering only one phase of the traction inverter, though the analysis is the same for all three phases.

The upper and lower charging stages generate a voltage,  $v_{chg,a1}(t)$  and  $v_{chg,a2}(t)$ , respectively. As can be inferred from

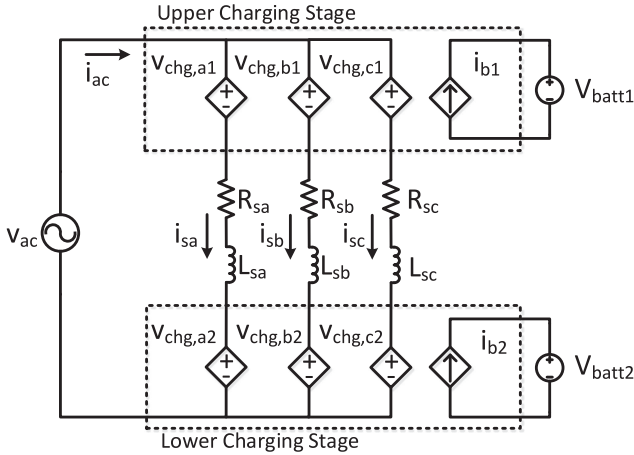


Fig. 7. Average model of the proposed system.

Fig. 6,

$$v_{chg,a1}(t) = v_{g,1}(t) - v_{a,1}(t) \quad (1)$$

$$v_{chg,a2}(t) = v_{g,2}(t) - v_{a,2}(t). \quad (2)$$

In other words, the charging stage voltage is a function of the voltage produced by the grid stage as well as the traction inverter. Note that this allows for the charging stage voltage to be bipolar in nature.

By using the intuition obtained from Fig. 6, the average model of the system can be developed, as shown in Fig. 7. It can be seen that the upper and lower charging stages are effectively series connected. This implies that the voltage produced by the charger is not limited by an individual battery voltage but by the sum of both batteries in the drivetrain. Therefore, the proposed on-board integrated charger is able to connect to higher voltage systems as compared to on-board integrated chargers based on standard 450-V drivetrains, which are limited by their single battery. As mentioned, each phase of the traction inverter is identically modulated. This results in the following:

$$v_{chg,a1}(t) = v_{chg,b1}(t) = v_{chg,c1}(t) \quad (3)$$

$$v_{chg,a2}(t) = v_{chg,b2}(t) = v_{chg,c2}(t). \quad (4)$$

It is clear from the average model why this condition is required to prevent torque production. If the charging stage voltages are equal, then given a symmetrical machine, only zero-sequence currents will flow within the machine, producing no torque. Note that (3) and (4) imply the following:

$$S_{a1} = S_{b1} = S_{c1} \quad (5)$$

$$S_{a2} = S_{b2} = S_{c2}. \quad (6)$$

Henceforth,  $v_{chg,1}(t)$  and  $v_{chg,2}(t)$  will be used to represent the upper and lower charging stage voltages, while  $S_1$  and  $S_2$  will represent the gating signals sent to the traction inverters of the upper and lower charging stages, respectively.

The bipolar charging stage voltages are defined as follows:

$$v_{chg,1}(t) = m_1(t)V_{Batt1} \quad (7)$$

$$v_{chg,2}(t) = m_2(t)V_{Batt2} \quad (8)$$

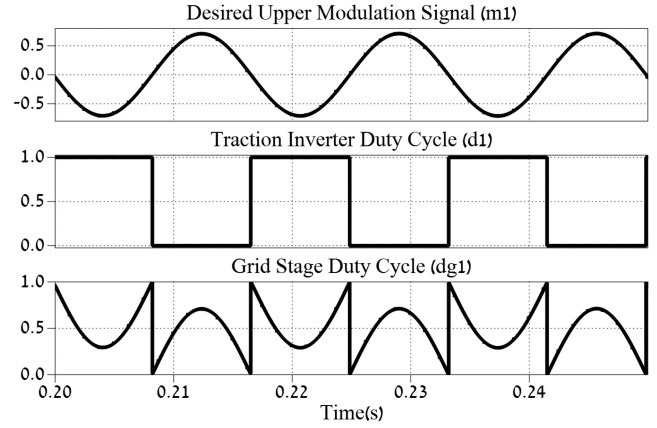


Fig. 8. Visual representation of (12) using an exemplary modulation signal.

where  $m_1(t)$  and  $m_2(t)$  are conventional ac modulation signals. They are outputs of the controller (described later) and are real valued, ranging from  $-1$  to  $1$ . As the charging stage voltage is defined by the grid stage as well as the traction inverter, the desired modulation signal cannot directly control a set of switches. Rather, it must be decomposed into two separate modulation signals for the grid stage and traction inverter. Considering only the upper charging stage, (1) can be rewritten in terms of modulation signals as follows:

$$m_1(t)V_{Batt1} = d_{g,1}(t)V_{Batt1} - d_1(t)V_{Batt1} \quad (9)$$

where  $d_{g,1}(t)$  is the duty cycle used to generate the gating signal  $S_{g,1}$  and  $d_1(t)$  is the duty cycle used to generate the gating signal  $S_1(t)$ . Dividing (9) by  $V_{Batt1}$  yields the following relationship:

$$m_1(t) = d_{g,1}(t) - d_1(t). \quad (10)$$

In order to generate a bipolar voltage,  $d_1(t)$  can be assigned such that

$$d_1(t) = \begin{cases} 0 & V_{ac} \geq 0 \\ 1 & V_{ac} < 0. \end{cases} \quad (11)$$

This effectively utilizes the traction inverter as an inverting or unfolding stage, which only has to switch at the grid frequency (60 Hz), thus minimizing switching loss in the high-power traction inverter.

Finally, rearranging (10) will allow us to calculate the duty cycle of the grid stage as follows:

$$d_{g,1}(t) = m_1(t) + d_1(t). \quad (12)$$

An equivalent set of equations may be written for the lower charging stage. A visualization of this is provided in Fig. 8, where it can be seen how the grid stage duty cycle  $d_{g,1}(t)$  is derived from the modulation index ( $m_1$ ) and the traction inverter duty cycle ( $d_1$ ). Also note that the traction inverter duty cycle ( $d_1$ ) can be directly translated to its corresponding gating signal ( $S_1$ ), while the grid stage duty cycle ( $d_{g1}$ ) requires a pulsewidth modulation. In summary, this modulation scheme

TABLE II  
INTEGRATED CHARGER SWITCHING STATES

State	$S_{g,1}$	$S_{g,2}$	$S_1$	$S_2$	$V_{out}$
a	0	0	0	0	0
b	0	0	0	1	$-V_{batt2}$
c	0	0	1	0	$-V_{batt1}$
d	0	0	1	1	$-V_{batt1} - V_{batt2}$
e	0	1	0	0	$V_{batt2}$
f	0	1	0	1	0
g	0	1	1	0	$V_{batt2} - V_{batt1}$
h	0	1	1	1	$-V_{batt1}$
i	1	0	0	0	$V_{batt1}$
j	1	0	0	1	$V_{batt1} - V_{batt2}$
k	1	0	1	0	0
l	1	0	1	1	$-V_{batt2}$
m	1	1	0	0	$V_{batt1} + V_{batt2}$
n	1	1	0	1	$V_{batt1}$
o	1	1	1	0	$V_{batt2}$
p	1	1	1	1	0

can decompose the output of the controller into gating signals for the grid stage, and the traction inverter, such that each charging stage outputs a bipolar voltage, while the traction inverter only switches at the grid frequency.

Note that this decomposition differs from that presented in [1] in that the roles of the grid stage and the traction inverter are reversed. The 60-Hz switching is now performed by the large traction inverter, while the high frequency switching is done by the grid stage. This is advantageous since the traction inverter is designed for optimal operation of the drive, while the grid stage can be specifically chosen for the charging system. Specifically, the charging efficiency over the desired range of operation can be controlled by choosing appropriate semiconductors for the grid stage. This is a degree of freedom not offered by the aforementioned integrated chargers in literature.

The multilevel nature of this charger can be visualized by looking at Table II, where the voltage output of each switching state is listed. Note that it is based on the simplified schematic shown in Fig. 6. Due to the constraint imposed by (11), the converter traverses through a subset of the total switching states. Specifically, the converter will only traverse states where  $S_1 = S_2$ ; therefore, during operation, the converter traverses through the switching states  $\{a, d, e, h, i, l, m, p\}$ . The operating mode described in [1] traverses through the set of states  $\{a, b, c, d, m, n, o, p\}$ . Using Table II, it can be shown that both sets of switching states produce the same set of output voltages; thus, it is possible to operate with increased system efficiency without changing the fundamental operation of the charger. It is also worthy to note that the states traversed effectively produce a five-level output from the charger, which is the key enabler in operating with low total harmonic distortion (THD), while only using the relatively small inherent inductance of a real EV traction motor. This is summarized in Fig. 9, where the resulting five-level waveform can be seen.

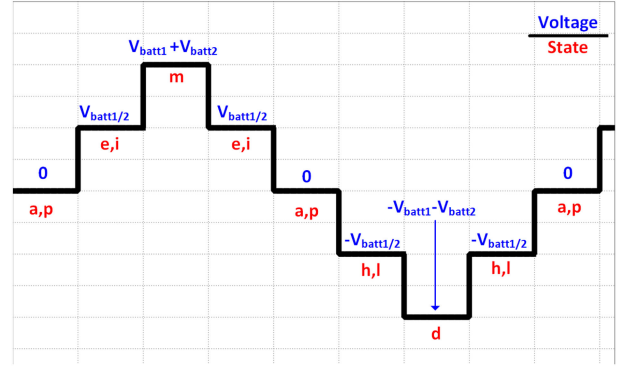


Fig. 9. Visual representation of the switching states traversed during operation which results in a five-level output voltage.

### B. Energy Balancing

In such a drive system, two separate energy storage units are required, which may be batteries, supercapacitors, fuel cells, or any combination thereof. In this article, batteries are used; however, a method for balancing the individual charging rates is required to ensure even charging. This can be achieved by asymmetrically modulating the upper and lower charging stages. However, it is best to first describe the system's nominal operation using the average model shown in Fig. 7. In the model, each phase of the charging stage is represented by a bipolar variable voltage source, as defined by (7) and (8).

Both the upper and lower charging stage voltages, neglecting voltage drop across the motor impedances, are equal to  $\frac{v_{ac}(t)}{2}$  as described in Section II-A. Therefore, the power into the upper and lower charging stages is equal to

$$P_1 = \text{Re} \left\{ \frac{V_{ac}}{2} I_{ac}^* \right\} \quad (13)$$

$$P_2 = \text{Re} \left\{ \frac{V_{ac}}{2} I_{ac}^* \right\} \quad (14)$$

where  $V_{ac}$  is the rms phasor of  $v_{ac}(t)$  and  $I_{ac}$  is the rms phasor of  $i_{ac}(t)$ . As can be seen, the upper and lower charging stages nominally receive equal power.

The proposed on-board integrated charger can balance energy between the batteries of upper and lower charging stages by modifying the relative voltages between the upper and lower charging stages by a given increment  $\delta(t)$  as shown in the following equations:

$$v_{chg,1}(t) = (1 - \delta(t))M_1(t)V_{batt1} \quad (15)$$

$$v_{chg,2}(t) = (1 + \delta(t))M_2(t)V_{batt2}. \quad (16)$$

The resulting power of the upper and lower charging stages are now unequal as seen in the following equations:

$$P_1 = \text{Re} \left\{ \frac{(1 - \delta(t))V_{ac}}{2} I_{ac}^* \right\} \quad (17)$$

$$P_2 = \text{Re} \left\{ \frac{(1 + \delta(t))V_{ac}}{2} I_{ac}^* \right\}. \quad (18)$$

As the combined voltage of the upper and lower charging stages is independent of  $\delta(t)$ , the system is able to balance energy between the upper and lower charging stages without affecting grid side power transfer.

### C. Maximum Charging Power

The maximum charging power of this integrated OBC is limited by the sum of the battery voltages (at their lowest SoC) and the inherent current rating of the traction motor. The maximum grid current is related to the machine's phase current rating by

$$I_{\text{grid,max}} = 3I_{\text{phase,max}}. \quad (19)$$

Since the grid current can be three times larger than the maximum per phase current rating of the machine, this implies that very large grid currents can be attained even with a relatively modest EV machine. For example, a machine with 100-A current rating can allow a grid current of up to 300 A. One of the key advantages of the proposed charger is its ability to operate at higher grid voltages, even though it is still technically operating as a boost-type converter. Based on the sum of the battery voltages, the maximum grid voltage can be determined as follows:

$$V_{\text{grid,rms}} \leq \frac{V_{\text{Batt1,min}} + V_{\text{Batt2,min}}}{\sqrt{2}} \quad (20)$$

Considering a dual-inverter drivetrain with standard 450-V batteries at a low SoC, i.e.,  $V_{\text{Batt}} = 350$  V, the highest voltage grid that can be connected according to (20) would be  $V_{\text{grid}} = 496 V_{\text{rms}}$ . Looking at commonly available grid voltage levels, this means the charger is able to directly interface with a 480 V grid. This allows the charger to charge up to 48-kW (defined as the product of grid voltage and current) when drawing only 100  $A_{\text{rms}}$ . Previously proposed solutions would be limited to charging from at most  $V_{\text{grid}} = 240 V_{\text{rms}}$  or effectively at half the power.

## III. CONTROL SCHEME

The on-board integrated charger must enable charging of the EV battery and satisfy the THD requirements of the grid. Despite the small leakage inductance of the EV motor, this is readily achievable by leveraging the multilevel operation of the charger and by sizing the grid stage semiconductors for the required charging current.

A high-level control scheme suitable for this system is shown in Fig. 10. To control the currents, a set of resonant current controllers ( $G_{\text{PR}}$ ) are used to ensure that the fundamental frequency current is regulated while significant harmonics (third, fifth, seventh, and ninth) are reduced. This makes for a relatively conventional and simple controller structure which is attributed to the developed modulation scheme described in Section II-A.

The energy balance controller introduces a  $\delta(t)$  reference as described in Section II-B. The  $\delta(t)$  reference is used to modify the average power delivered to the upper and lower charging stage batteries and is used to balance the energy between the upper and lower batteries. The  $\delta(t)$  reference is created using a

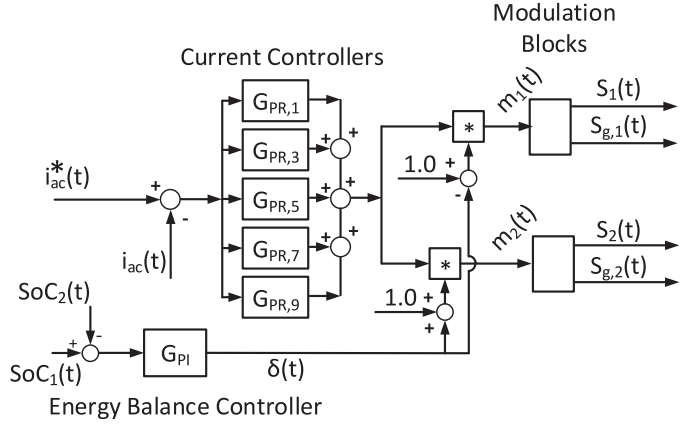


Fig. 10. Controller block diagram.

proportional-integral (PI) controller, which regulates the difference between the SoC of the upper and lower batteries.

A benefit to the proposed charger is that the current conducted through the motor's leakage inductance is a sinusoid at the grid frequency. In comparison, other PFC-type chargers use a diode rectifier front-end [9], [22], where the motor must conduct a rectified grid current. Tracking a rectified sinusoid can be difficult with high-power, insulated gate bipolar transistor (IGBT)-based traction inverters due to the high control bandwidth requirements (which also implies high switching frequencies). Also note that no reconfiguration logic is required since the system does not need any physical reconfiguration switchgear for charging.

### A. Power Factor Control

One of the features of this integrated charger is its ability to operate at any power factor. This means the system must have a notion of the phase associated with the grid voltage in order to drive a current at a specific phase offset. Specifically, the reference current that is generated must be controlled to be at a specific phase offset with respect to the grid voltage. The reference current can be generated based on the grid voltage by using a simple synchronizing oscillator described in [24]. In state space form, this oscillator is expressed as follows:

$$\begin{aligned} \begin{bmatrix} \dot{x}_1 \\ \dot{x}_2 \end{bmatrix} &= \begin{bmatrix} -k_{\text{sync}} & w_0 \\ -w_0 & 0 \end{bmatrix} \begin{bmatrix} x_1 \\ x_2 \end{bmatrix} + \begin{bmatrix} k_{\text{sync}} \\ 0 \end{bmatrix} v_{ac}, \\ \begin{bmatrix} v_{ac\parallel} \\ v_{ac\perp} \end{bmatrix} &= \begin{bmatrix} y_1 \\ y_2 \end{bmatrix} = \begin{bmatrix} 1 & 0 \\ 0 & 1 \end{bmatrix} \begin{bmatrix} x_1 \\ x_2 \end{bmatrix} \end{aligned} \quad (21)$$

where we have the following.

- 1)  $x_1, x_2$  and  $y_1, y_2$  are the oscillator states and outputs, respectively.
- 2)  $v_{ac\parallel}$  is a signal with the same amplitude, phase, and frequency as the fundamental of the grid voltage.
- 3)  $v_{ac\perp}$  is a signal with the same amplitude and frequency as the fundamental of the grid voltage, with a  $90^\circ$  phase shift.
- 4)  $w_0$  is the nominal frequency of the grid voltage and is set to 377 rad/s.

TABLE III  
SIMULATION PARAMETERS

Integrated Charger Parameters	Symbol	Value
Machine phase resistance	$R_s$	$45m\Omega$
Machine leakage inductance	$L_s$	$0.5mH$
Battery voltage	$V_{batt1}, V_{batt2}$	$400V$
X capacitor	$C_x$	$20 \mu F$
Grid stage switching frequency	$f_{sw}$	$20kHz$
Traction inverter switching frequency	$f_{sw,inv}$	$60Hz$
Grid Parameters	Symbol	Value
Grid Voltage	$V_{ac}$	$240/480V_{rms}$
Grid Current	$I_{ac}$	$60A_{rms}$

5)  $k_{sync}$  is the damping factor of the oscillator and is set to 1000.

The signals  $v_{ac\parallel}$  and  $v_{ac\perp}$  can be normalized according to

$$\hat{u}_{ac\parallel} = \frac{v_{ac\parallel}}{\sqrt{v_{ac\parallel}^2 + v_{ac\perp}^2}}, \quad \hat{u}_{ac\perp} = \frac{v_{ac\perp}}{\sqrt{v_{ac\parallel}^2 + v_{ac\perp}^2}} \quad (22)$$

where  $\hat{u}_{ac\parallel}$  is a normalized signal with the same frequency and phase as the grid and  $\hat{u}_{ac\perp}$  is a normalized signal with same frequency as the grid but with a  $90^\circ$  phase shift. Finally, these normalized signals can be used to generate a sinusoidal ac current reference  $i_{ac}^*(t)$  with any phase shift and amplitude according to

$$i_{ac}^*(t) = I_{ref}(\hat{u}_{ac\parallel}\cos(\gamma) + \hat{u}_{ac\perp}\sin(\gamma)) \quad (23)$$

where  $\gamma$  specifies the desired phase offset from the grid voltage and  $I_{ref}$  specifies the desired peak value of the ac charging current.

#### IV. SIMULATION RESULTS

The single-phase integrated charger is implemented as a full switch model in PLECS in order to demonstrate its full range of operation, namely operation using a high-voltage machine. The simulation parameters used are shown in Table III.

Exemplary waveforms of the proposed charger operating at unity power factor when connected to a  $480-V_{rms}$  grid are provided in Fig. 11. The waveforms show the grid stage and traction inverter phase voltages, which comprise the overall upper charging stage's ac voltage as described in (1). As previously discussed, the upper charging stage is expected to output a voltage approximately half of that of  $v_{ac}(t)$ . Charging operation is also shown when the charger is connected to a  $240-V_{rms}$  grid in Fig. 12. It can be seen that the ripple shape of the phase currents are different when compared to the  $480-V_{rms}$  case. This is due to the fact that the  $240-V_{rms}$  operation does not require all the five output voltage levels shown in Fig. 9 since the grid voltage is relatively low compared to the sum of the battery voltages.

Due to (3) and (4), the currents in each phase of the motor are equal. Therefore, all phase voltages are equal, given a symmetrical machine. In consequence, Fig. 11 shows that  $i_{sa}(t)$ ,  $i_{sb}(t)$ , and  $i_{sc}(t)$  contribute one-third of  $i_{ac}(t)$ . These equal currents represent a zero sequence set and the machine produces no

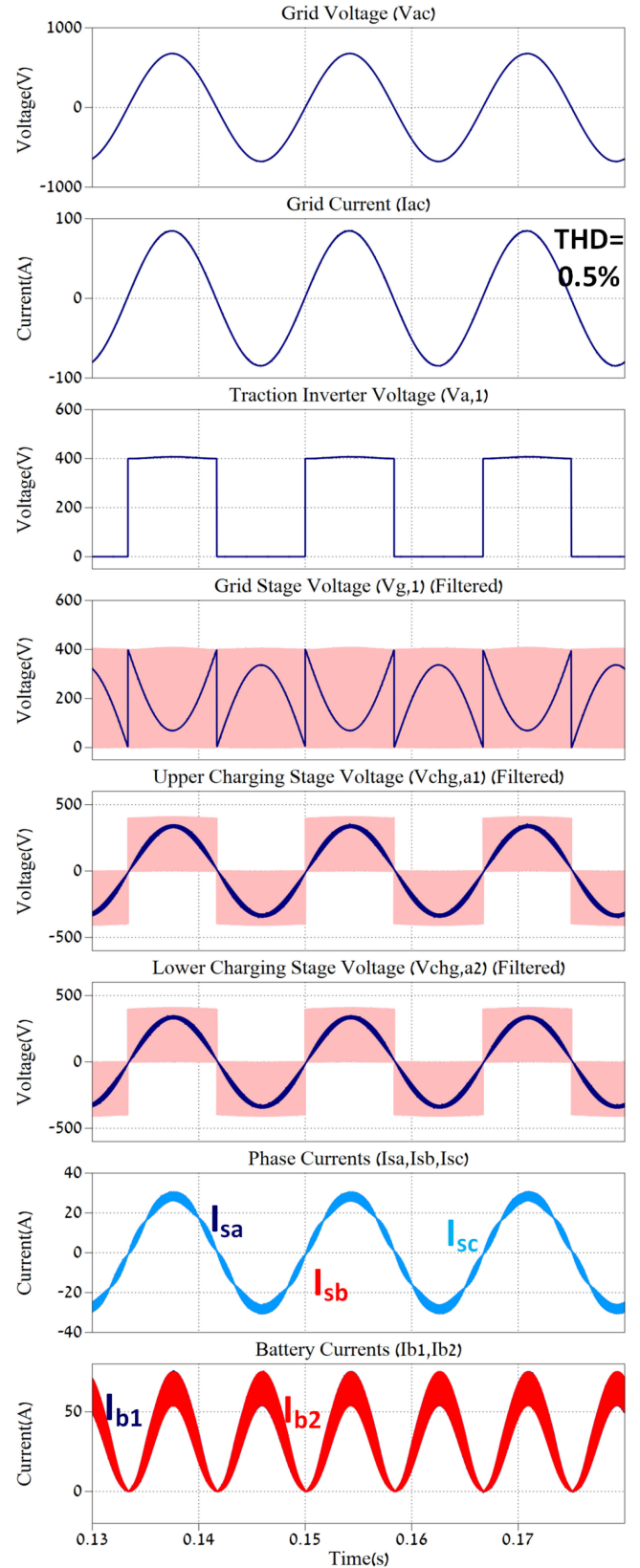


Fig. 11. Steady-state simulation results when connected to a  $480-V_{rms}$  grid. Note that the phase currents ( $I_{sa}, I_{sb}, I_{sc}$ ) and battery currents ( $I_{b1}, I_{b2}$ ) are identical, thus completely overlapping.

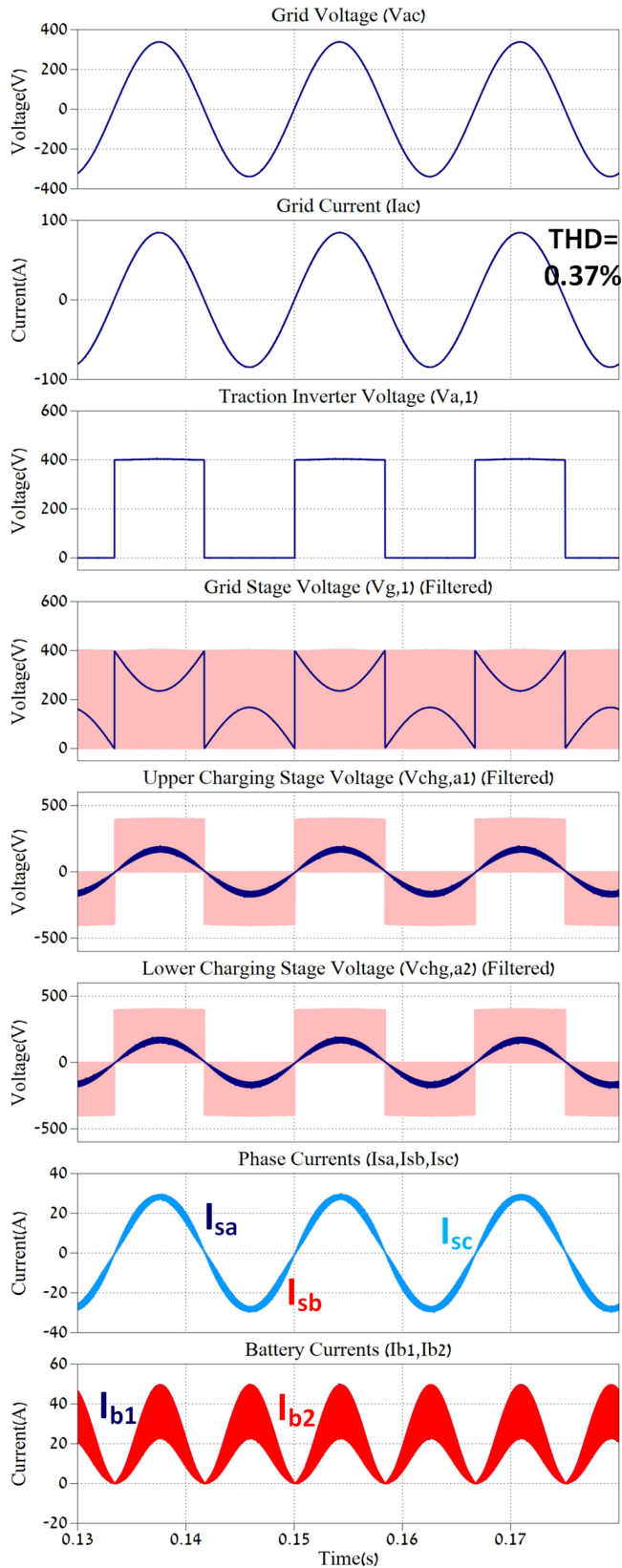


Fig. 12. Steady-state simulation results when connected to a 240- $V_{rms}$  grid. Note that the phase currents ( $I_{sa}$ ,  $I_{sb}$ ,  $I_{sc}$ ) and battery currents ( $I_{b1}$ ,  $I_{b2}$ ) are identical, thus completely overlapping.

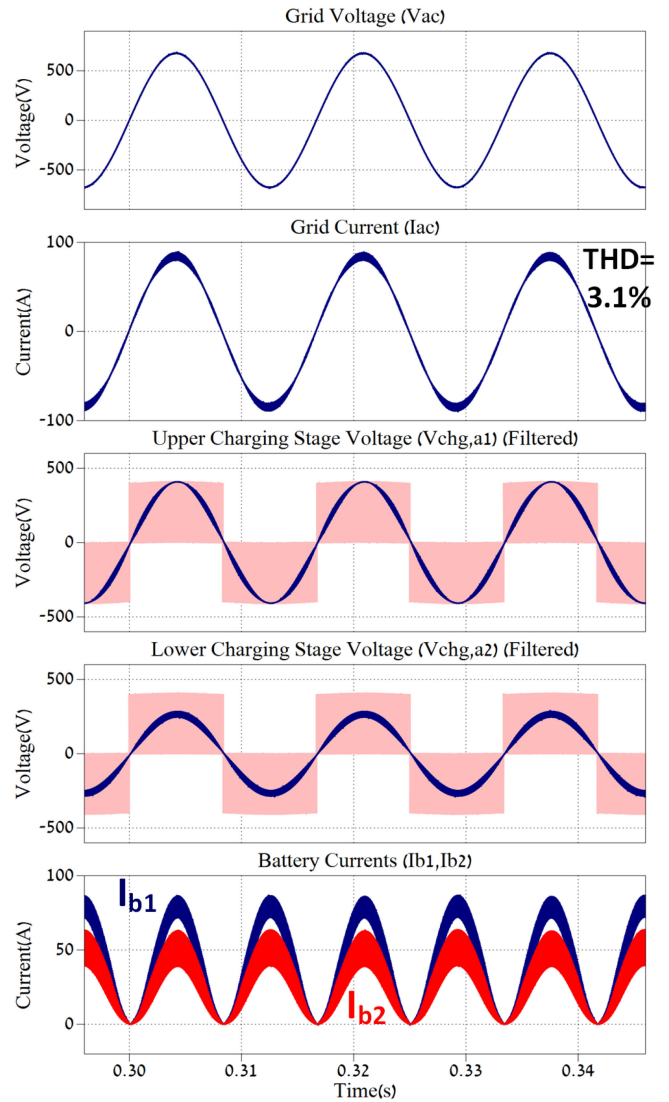


Fig. 13. Simulation results employing energy balancing.

average torque. Note that the machine currents are sinusoidal, as opposed to the rectified sinusoid in PFC-type chargers. Thus, this arrangement is suitable for stationary charging of the batteries.

Energy balancing is shown in Fig. 13, where the upper charging stage contributes more than half of grid voltage, as per (15), which consequently results in a higher current entering the battery of the upper charging stage. It can also be seen that this increases the ripple on the grid current, increasing THD from 0.5% to 3.1%. However, given that identical battery packs are used, such a large balancing current will not be required.

As shown in Fig. 11, the battery currents also exhibit the characteristic second harmonic current ripple present in any single-phase ac systems. A study conducted on lithium ion batteries shows that this has a negligible impact on the lifetime and performance of the battery [25]. In fact, Uno and Tanaka [26] noted that significant deterioration only occurs at frequencies

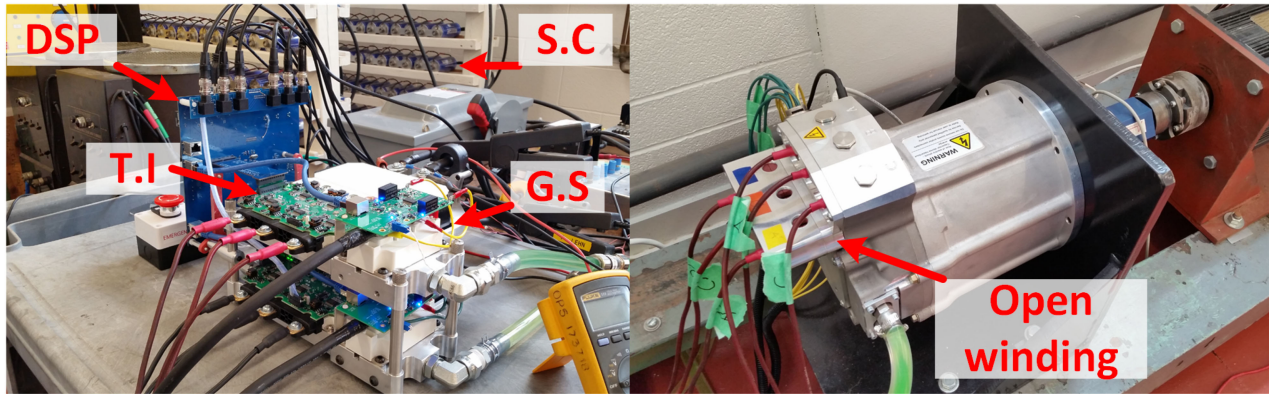


Fig. 14. Experimental setup with two charging stages consisting of a traction inverter (T.I), grid stage (G.S), controller board (DSP), open wound PM machine, and dual supercapacitor (S.C) banks emulating batteries.

TABLE IV  
EXPERIMENTAL PARAMETERS

Integrated Charger Parameters	Symbol	Value
Machine phase resistance	$R_s$	$45m\Omega$
Machine leakage inductance	$L_s$	$0.5mH$
Machine peak power	$P_m$	$110kW$
Battery voltage	$V_{batt1}, V_{batt2}$	$200V$
X capacitor	$C_x$	$20 \mu F$
Grid stage switching frequency	$f_{sw}$	$20kHz$
Traction inverter switching frequency	$f_{sw,inv}$	$60Hz$
Grid parameters	Symbol	Value
<b>Case A: Convenience Charge</b>		
Grid voltage	$V_{ac}$	$120V_{rms}$
Grid current	$I_{ac}$	$16A_{rms}$
Average Power	$P_{avg}$	$1.92kW$
<b>Case B: Opportunity Charge</b>		
Grid voltage	$V_{ac}$	$240V_{rms}$
Grid current	$I_{ac}$	$30A_{rms}$
Average Power	$P_{avg}$	$7.2kW$
<b>Case C: Quick Charge</b>		
Grid voltage	$V_{ac}$	$240V_{rms}$
Grid current	$I_{ac}$	$80A_{rms}$
Average Power	$P_{avg}$	$19.2kW$

below 10 hz since higher frequency harmonics merely serve to charge and discharge the double layer capacitance of the cell. Therefore, as long as the batteries are kept within the required temperature range, no additional degradation in the lifespan or performance will result from the second harmonic ripple associated with single-phase charging. In fact, battery chargers are being proposed, which leverage this potential degree of freedom [27], [28].

## V. EXPERIMENTAL RESULTS

Three main practical charging (G2V) scenarios are considered that would be compatible with the J1772 standard; Case A (convenience charging) is the slowest form of charging, which would only be used where only a standard 120-V outlet is available. Case B (opportunity charging) would be the most common charging method for EV owners, as 240 V is widely accessible in residential areas. Case C (quick charging) would be possible in locations with upgraded wiring to support up to 80 A

to be drawn from a single-phase 240-V grid. These scenarios as well as the parameters of the experimental system are shown in Table IV. A picture of the experimental setup is shown in Fig. 14. In this case, a PM liquid cooled EV machine with an open stator connection was used; however, the system is also compatible with induction machines. Each charging stage consists of an Infineon FS820R08A6P2LB three-phase IGBT-based traction inverter, a Wolfspeed CAS300M12BM2 silicon carbide (SiC) based grid stage, and a 16.6-F supercapacitor bank which emulates the batteries. Steady-state results are shown in Fig. 15. As expected, convenience charging, shown in Fig. 15(a), from a 120-V grid is the worst case for THD since the fundamental current is low. The magnitude and shape of the machine current ripple is also different because of the larger difference between the battery voltage and grid voltage (as compared to 240-V charging). This phenomena can also be explained using the formulations in [21]. Operations at 30 and 80  $A_{rms}$  are shown in Fig. 15(b) and (c), respectively.

It can be seen that THD is less than the 5% requirement of the IEEE 519 standard. It is also important to note that there is no movement of the machine during charging. The battery current exhibits the expected second harmonic ripple as well as a small 60-Hz harmonic seen under low current charging (Fig. 15(a)). This harmonic does not increase with charging power; therefore, it becomes less visible as the charging power increases. This is due to the asymmetrical (sawtooth) modulation scheme utilized for the experimental setup, which produces a small third harmonic component in the grid current. Simulation results do not exhibit this since symmetrical (triangular) modulation is used.

### A. Transient Response

Three transient tests are conducted to verify the proper operation of the implemented controllers. The current controllers were tested by applying a 30-A step in the reference current. The result is shown in Fig. 16. It can be seen that the current reaches the set-point within one line cycle. The power factor control was tested by stepping the power factor from unity to 0.5 leading. The result is shown in Fig. 17, where the power factor changes in a fraction of a line cycle. Finally, a test was conducted to verify

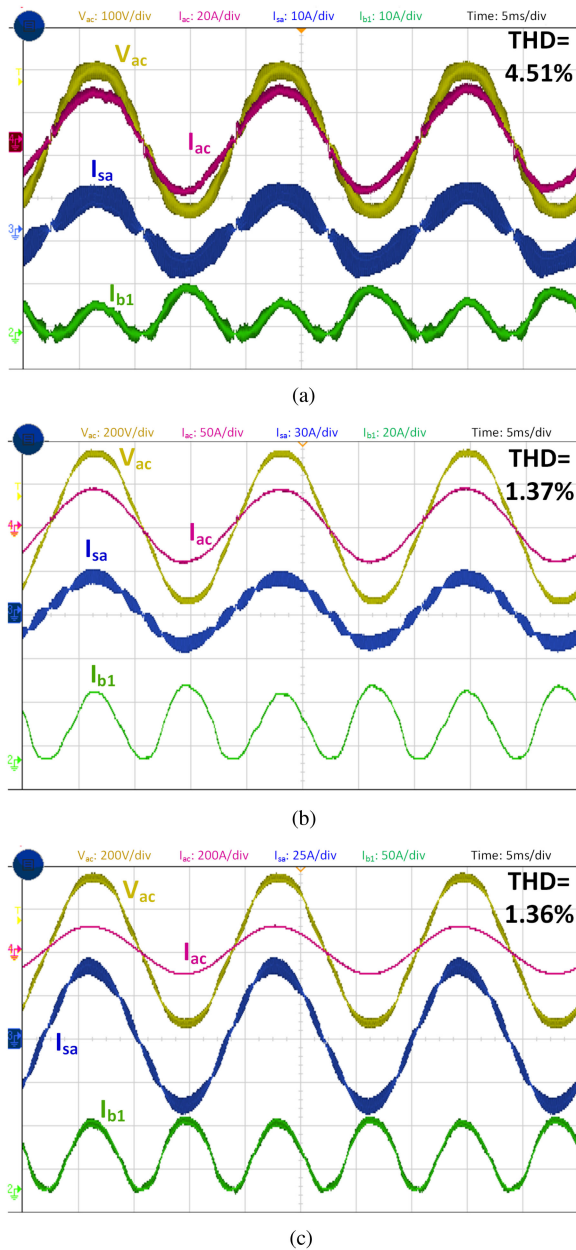


Fig. 15. Steady-state experimental results, G2V at unity PF. (a) Case A: Convenience charge, 16  $A_{rms}$  at 120 V. (b) Case B: Opportunity charge, 30  $A_{rms}$  at 240 V. (c) Case C: Quick charge, 80  $A_{rms}$  at 240 V.

the system's ability to transition to and from V2G mode (power factor of 1 generating).

This is shown in Fig. 18, where it can be seen that the transitions take only one line cycle. Note that during any of these transient tests, the battery currents, phase currents, and the grid current do not exhibit any undesirable transient artifacts.

### B. Discharging (V2G) Operation

If the current is set to be  $180^\circ$  out of phase with the voltage, then the integrated charger will deliver maximum power back into the grid, operating in V2G mode. This is shown in Fig. 19, where the power factor is measured to be unity (generating),

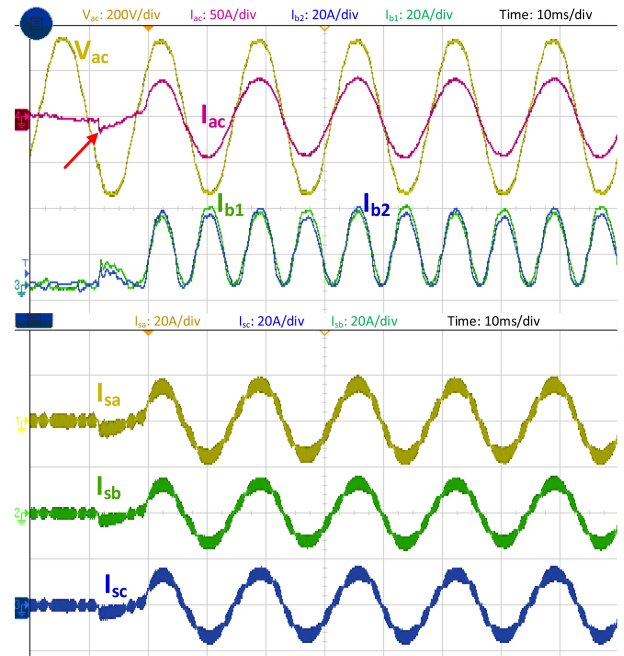


Fig. 16. Transient response to a current step from 0 to 30  $A_{rms}$  at unity PF. Arrow indicates start of transient event.

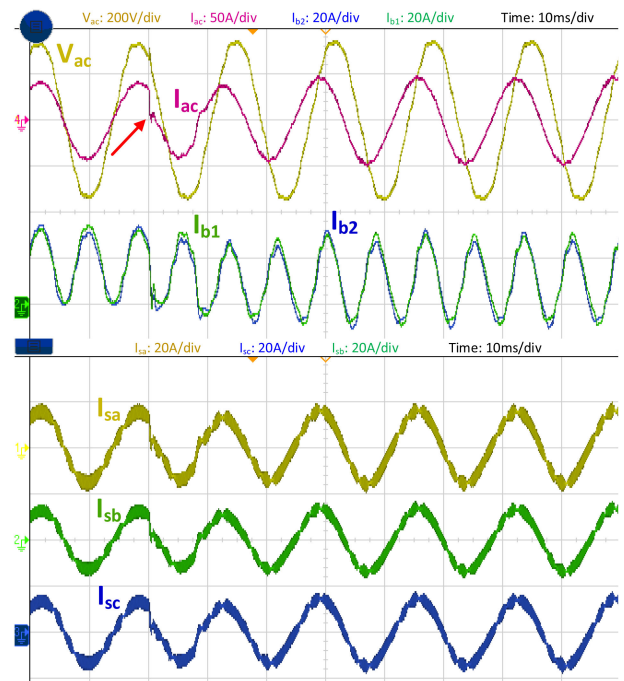


Fig. 17. Transient response to a step in PF from 1 to 0.5 leading at 30  $A_{rms}$ . Arrow indicates start of transient event.

and the battery currents are completely negative. The overall operation and performance of the system is unchanged, except that the ac currents in the system are phase shifted.

### C. Efficiency Measurements

The operating efficiency of any charger is critical for determining its feasibility in real-world applications. As such,

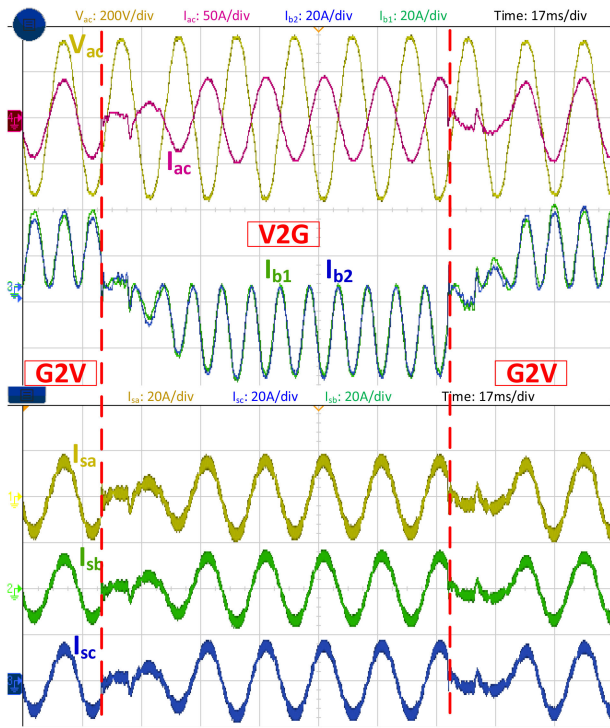


Fig. 18. Transient response of system switching from G2V and V2G and vice versa.

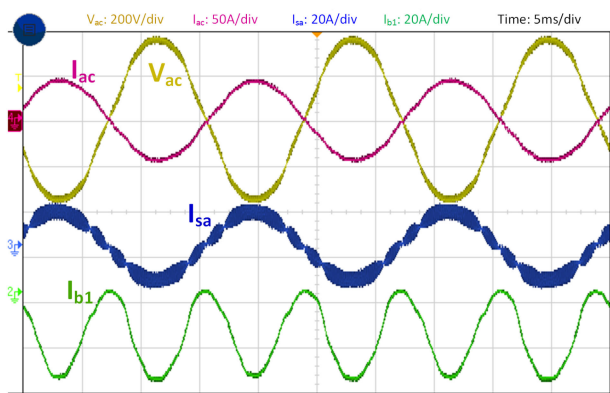


Fig. 19. Steady-state experimental result, V2G at unity PF.

an efficiency measurement was conducted for the proposed integrated charger under both charging (G2V) and discharging (V2G) operation with the system parameters in Table IV. The results are shown in Fig. 20. It can be seen that a relatively flat efficiency around 96% and 97.5% is achieved during charging and discharging, respectively, at the power levels expected for the majority of operation. This verifies that the concept of integrated charging is viable from an efficiency perspective. As expected, the efficiency suffers at light loads; however, this can be improved by employing advanced light load switching strategies, such as adaptive on-time control [29]. An interesting characteristic is that the discharging efficiency is slightly higher than the charging efficiency. This can be attributed to the fact that during charging, the phase currents must travel

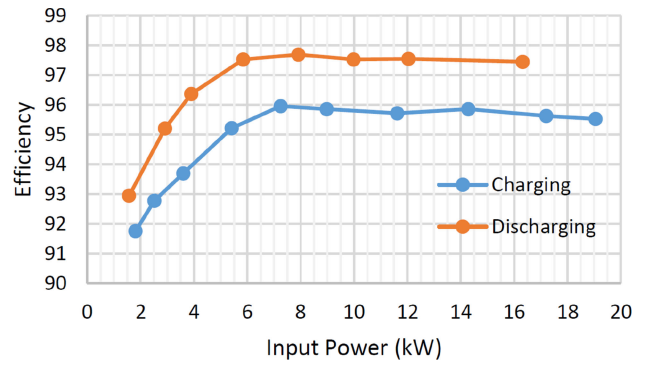


Fig. 20. Integrated charger efficiency, operating from a 240V<sub>ac</sub> grid with each battery at 200 V.

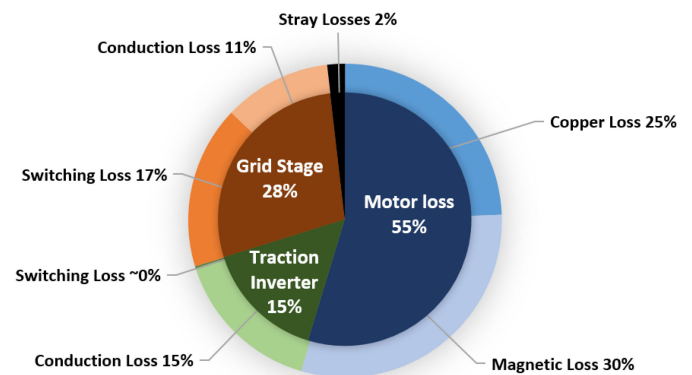


Fig. 21. Loss breakdown of integrated charger at 10-kW input power.

through the antiparallel diode of the traction inverter, while during discharging, the current passes through the lower loss IGBTs of the traction inverter. In the future, the use of SiC MOSFET based drives would avoid diode conduction during charging and its associated efficiency penalty. A breakdown of the system losses is presented in Fig. 21. It can be seen that a large portion of the loss is attributed to the motor losses, which was experimentally measured. Since the motor is optimized for processing much higher powers, it makes sense that at lower powers, the motor becomes the dominant source of loss. Finally, as expected, the traction inverter has virtually no switching loss since it is switching only during the zero crossing points of the current at a low frequency of 60 Hz.

#### D. Driving Mode

The operation of the dual-inverter system as a conventional drive has been investigated in the past [30]–[32]. However, in order to demonstrate that the additional components added for charging operation do not hinder motoring operation, a simple experimental test was conducted. In Fig. 22, a 30-Nm torque step was applied to the EV machine. Here, the EV machine is mechanically coupled to a dynamometer with a resistive load. It can be seen that the dual-inverter drive operates as expected.

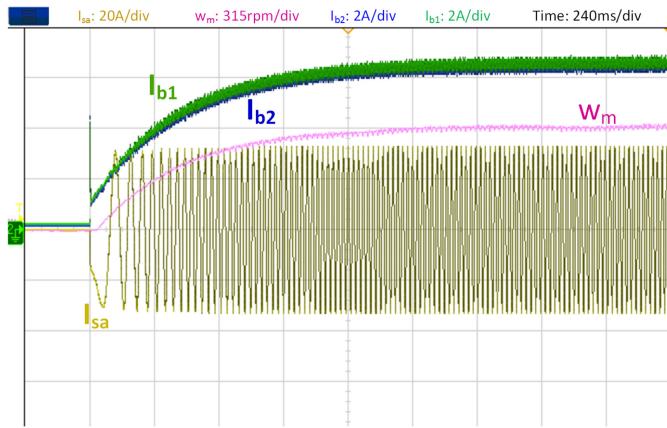


Fig. 22. Demonstration of motoring operation with an applied torque step of 30 Nm.

## VI. CONCLUSION

This article presents a single-phase integrated OBC based on the dual-inverter drive. By leveraging pre-existing high-power components of the drivetrain, it is possible to charge the batteries of the EV directly from a single-phase grid, at power levels surpassing current state-of-the-art discrete OBCs. An AFE reduces control bandwidth requirements (and consequently switching frequency requirements) as it allows the conducted current to be a sinusoid at grid frequency, as opposed to a rectified sinusoid. It also allows V2G operation of the charger, at any power factor, thus making the EV capable of grid support functionalities, such as voltage support, frequency regulation, and peak shaving, in addition to charging.

Simulation results show that the proposed charger equipped with two standard 400-V battery packs can directly charge from a 480-V grid while allowing control over the individual charging rates of each battery. Experimental results demonstrated charging and V2G operation up to 19.2 kW using a 110-kW PM EV machine and associated power electronics, without creating any rotation or torque in the machine itself. It was also shown that grid THD requirements are met for a wide operating range (1.92–19.2 kW). Measured system efficiencies reaching over 97% validate the efficacy of the proposed modulation scheme for reducing switching losses in the large traction inverters.

## APPENDIX

This section contains transfer function and gains of the PR controllers shown in Fig. 10, as follows:

$$G_{PR,1} = \frac{0.51670 s^2 + 168.9472 s + 32712.42}{s^2 + 0.754 s + 142129} \quad (24)$$

$$G_{PR,3} = \frac{0.51670 s^2 + 168.9472 s + 32712.42}{s^2 + 2.262 s + 1279161} \quad (25)$$

$$G_{PR,5} = \frac{0.51670 s^2 + 168.9472 s + 32712.42}{s^2 + 3.77 s + 3553225} \quad (26)$$

$$G_{PR,7} = \frac{0.51670 s^2 + 168.9472 s + 32712.42}{s^2 + 5.278 s + 6964321} \quad (27)$$

$$G_{PR,9} = \frac{0.51670 s^2 + 168.9472 s + 32712.42}{s^2 + 6.786 s + 11512449} \quad (28)$$

## ACKNOWLEDGEMENT

We acknowledge the support of the Natural Sciences and Engineering Research Council of Canada (NSERC), [funding Ref. No. CRDPJ 513206 - 17].

## REFERENCES

- [1] T. Soong and P. W. Lehn, "On-board single-phase electric vehicle charger with active front end," in *Proc. Int. Power Electron. Conf. (IPEC-Niigata ECCE Asia)*, May 2018, pp. 3203–3208.
- [2] M. Yilmaz and P. T. Krein, "Review of battery charger topologies, charging power levels, and infrastructure for plug-in electric and hybrid vehicles," *IEEE Trans. Power Electron.*, vol. 28, no. 5, pp. 2151–2169, May 2013.
- [3] W. E. Rippel and A. G. Cocconi, "Integrated motor drive and recharge system," U.S. Patent 5099186A, Mar. 24, 1992.
- [4] S. J. Lee and S. K. Sul, "An integral battery charger for 4 wheel drive electric vehicle," in *Proc. IEEE Ind. Appl. Soc. Annu. Meet.*, Oct. 1994, vol. 1, pp. 448–452.
- [5] D. J. McShane, "Combined drive/chargers for electric vehicles: Advanced technology to "side-step" the batteries," in *Proc. IEE Colloq. Adv. Control Syst. Electric Drives*, May 1995, pp. 1/1–1/7.
- [6] I. Subotic, E. Levi, M. Jones, and D. Graovac, "On-board integrated battery chargers for electric vehicles using nine-phase machines," in *Proc. IEEE Int. Electric Mach. Drives Conf.*, May 2013, pp. 226–233.
- [7] I. Subotic and E. Levi, "A review of single-phase on-board integrated battery charging topologies for electric vehicles," in *Proc. IEEE Workshop Elect. Mach. Des., Control Diagnosis*, Mar. 2015, pp. 136–145.
- [8] L. De-Sousa and B. Bouchez, "Combined electric device for powering and charging," U.S. Patent 20110221363A1, Dec. 17, 2013.
- [9] G. Pellegrino, E. Armando, and P. Guglielmi, "An integral battery charger with power factor correction for electric scooter," *IEEE Trans. Power Electron.*, vol. 25, no. 3, pp. 751–759, Mar. 2010.
- [10] L. Tang and G. J. Su, "A low-cost, digitally-controlled charger for plug-in hybrid electric vehicles," in *Proc. IEEE Energy Convers. Congr. Expo.*, Sep. 2009, pp. 3923–3929.
- [11] I. Subotic, N. Bodo, and E. Levi, "Single-phase on-board integrated battery chargers for EVs based on multiphase machines," *IEEE Trans. Power Electron.*, vol. 31, no. 9, pp. 6511–6523, Sep. 2016.
- [12] J. Hong, H. Lee, and K. Nam, "Charging method for the secondary battery in dual-inverter drive systems for electric vehicles," *IEEE Trans. Power Electron.*, vol. 30, no. 2, pp. 909–921, Feb. 2015.
- [13] Y. Hu, C. Gan, W. Cao, C. Li, and S. Finney, "Split converter-fed SRM drive for flexible charging in EV/HEV applications," *IEEE Trans. Ind. Electron.*, vol. 62, no. 10, pp. 6085–6095, Oct. 2015.
- [14] S. Loudot, B. Briane, O. Ploix, and A. Villeneuve, "Rapid reversible charging device for an electric vehicle," U.S. Patent 8 847 555B2, Dec. 23, 2014.
- [15] B. Brian and S. Loudot, "Rapid reversible charging device for an electric vehicle," U.S. Patent 20 110 254 494A1, Oct. 20, 2011.
- [16] D. Casadei, G. Grandi, A. Lega, and C. Rossi, "Multilevel operation and input power balancing for a dual two-level inverter with insulated DC sources," *IEEE Trans. Ind. Appl.*, vol. 44, no. 6, pp. 1815–1824, Nov.–Dec. 2008.
- [17] M. Mengoni, A. Amerise, L. Zarri, A. Tani, G. Serra, and D. Casadei, "Control scheme for open-ended induction motor drives with a floating capacitor bridge over a wide speed range," *IEEE Trans. Ind. Appl.*, vol. 53, no. 5, pp. 4504–4514, Sep.–Oct. 2017.
- [18] BRUSAa. NLG664 [Online]. Available: <https://www.brusa.biz/en/products/charger/charger-400-v/nlg664.html>
- [19] Motortrend. 2012 tesla model S first drive [Online]. Available: <https://www.motortrend.com/news/2012-tesla-model-s-first-drive/>
- [20] Renault. Battery and charging [Online]. Available: <https://www.renault.co.uk/vehicles/new-vehicles/zoe/motor.html>
- [21] R. Shi, S. Semsar, and P. W. Lehn, "Constant current fast charging of electric vehicles via DC grid using dual inverter drive," *IEEE Trans. Ind. Electron.*, vol. 64, no. 9, pp. 6940–6949, Sep. 2017.

- [22] S. Semsar, T. Soong, and P. W. Lehn, "Integrated single-phase electric vehicle charging using a dual-inverter drive," in *Proc. IEEE Transp. Electrific. Conf. Expo.*, Jun. 2018, pp. 320–325.
- [23] S. Liu, S. Hahlbeck, T. Schoenen, and K. Hameyer, "An integrated on-board charger with direct grid connection for battery electrical vehicle," in *Proc. Int. Symp. Power Electron. Power Electron., Elect. Drives, Autom. Motion*, Jun. 2012, pp. 335–340.
- [24] X. Zong and P. W. Lehn, "Reactive power control of single phase grid tied voltage sourced inverters for residential PV application," in *Proc. IECON 38th Annu. Conf. IEEE Ind. Electron. Soc.*, Oct. 2012, pp. 696–701.
- [25] S. Bala, T. Tegnér, P. Rosenfeld, and F. Delince, "The effect of low frequency current ripple on the performance of a lithium iron phosphate (LFP) battery energy storage system," in *Proc. IEEE Energy Convers. Congr. Expo.*, Sep. 2012, pp. 3485–3492.
- [26] M. Uno and K. Tanaka, "Influence of high-frequency charge–Discharge cycling induced by cell voltage equalizers on the life performance of lithium-ion cells," *IEEE Trans. Veh. Technol.*, vol. 60, no. 4, pp. 1505–1515, May 2011.
- [27] H. Belkamel, K. Hyungjin, K. Beywongwoo, Y. Shin, and S. Choi, "Bi-directional single-stage interleaved totem-pole ac–dc converter with high frequency isolation for on-board EV charger," in *Proc. IEEE Energy Convers. Congr. Expo.*, Sep. 2018, pp. 6721–6724.
- [28] B. Kim, M. Kim, and S. Choi, "A reduced component count single-stage electrolytic capacitor-less battery charger with sinusoidal charging," in *Proc. IEEE 3rd Int. Future Energy Electron. Conf. ECCE Asia*, Jun. 2017, pp. 242–246.
- [29] Q. Li, F. C. Lee, M. Xu, and C. Wang, "Light load efficiency improvement for PFC," in *Proc. IEEE Energy Convers. Congr. Expo.*, Sep. 2009, pp. 3755–3760.
- [30] R. Shi, S. Semsar, and P. W. Lehn, "Coordinated power sharing for enhanced utilization of mixed energy storage media in dual-inverter electric vehicles," in *Proc. IEEE Int. Electric Mach. Drives Conf.*, May 2019, pp. 1586–1592.
- [31] R. Menon, S. S. Williamson, N. A. Azeez, and A. H. Kadam, "A fault tolerant modulation strategy for dual inverter traction drives," in *Proc. IEEE Energy Convers. Congr. Expo.*, Sep. 2019, pp. 5856–5861.
- [32] V. Oleschuk, R. Bojoi, G. Griva, and F. Profumo, "Dual inverter-fed traction drive with dc sources power balancing based on synchronized PWM," in *Proc. IEEE Int. Electric Mach. Drives Conf.*, May 2007, vol. 1, pp. 260–265.



**Sepehr Semsar** (Student Member, IEEE) received the B.A.Sc. degree in electrical engineering in 2016 from the University of Toronto, Toronto, ON, Canada, where he is currently working toward the Ph.D. degree in electrical engineering.

His research interests include power electronics, electric vehicle drivetrains and charging systems, and high-efficiency dc–dc/dc–ac converters.



**Theodore Soong** (Member, IEEE) received the B.A.Sc. degree in engineering science and the M.A.Sc. and Ph.D. degrees in electrical engineering from the University of Toronto, Toronto, ON, Canada, in 2009, 2012, and 2015, respectively.

From 2015 to 2016, he was with ABB Corporate Research in Sweden, as a Scientist in the field of power electronics. Afterwards, in 2017, he was with the University of Toronto Electric Vehicle Research Centre as a Senior Research Associate. Since 2018, he has been with ABB Power Grids as an R&D Engineer. His research interests include electric vehicles, integration of renewable resources to the grid, grid-connected energy storage, and modular converters.



**Peter W. Lehn** (Senior Member, IEEE) received the B.Sc. and M.Sc. degrees in electrical engineering from the University of Manitoba, Winnipeg, MN, Canada, in 1990 and 1992, respectively, and the Ph.D. degree from the University of Toronto, Toronto, ON, Canada, in 1999.

He joined the Faculty at the University of Toronto, in 1999. He spent six months as a Visiting Professor at the University of Erlangen-Nuremberg, in 2001. His research interests include HVdc technologies, grid integration of storage and renewables, power

electronics for electric vehicles, and theoretical analysis of power electronic systems.

Prof. Lehn has been an Editor for the IEEE TRANSACTIONS ON ENERGY CONVERSION from 2013 to 2019.